Research Article

Deformation and Fracturing Behaviors of Sandstone Disc Containing a Circular Inclusion under Diametrical Compression: Insights from Integrated SG and DIC Experiments

Rongshan Nie ⓘ,[1] Qiuhong Wu ⓘ,[2] Zhaofei Chu ⓘ,[3,4,5] and Lei Weng ⓘ[3,4,5]

[1]*China Coal Technology and Engineering Group Shenyang Research Institute,*
 State Key Laboratory of Coal Mine Safety Technology, Fushun 113122, China
[2]*Hunan Provincial Key Laboratory of Safe Mining Techniques of Coal Mines, Hunan University of Science and Technology,*
 Xiangtan 411201, China
[3]*State Key Laboratory of Water Resource Protection and Utilization in Coal Mining,*
 CHN Energy Shendong Coal Group Co., Ltd., Beijing 102211, China
[4]*National Institute of Clean-and-Low-Carbon Energy, Beijing 102211, China*
[5]*School of Civil Engineering, Wuhan University, Wuhan 430072, China*

Correspondence should be addressed to Lei Weng; leiweng@whu.edu.cn

Weak inclusions play a significant role in regulating the deformation and fracturing behavior of rock masses. In this study, sandstone specimens filled with circular inclusions were subjected to diametrical compression until failure. The local strain concentration intensity and cracking process at the rock-inclusion interface were specifically investigated using the integrated strain gauge (SG) and digital image correlation (DIC) techniques. The experimental results reveal that the presence of inclusions introduces more complex deformation and fracturing behaviors in the infilled sandstone specimens. The stiffness of the infilled sandstones, with either low-strength or high-strength inclusions, initially increases and then decreases as the inclusion diameter increases. The effective load-carrying capacity of the infilled sandstone is influenced by the competing effects of inclusion enhancement and hole weakening. Moreover, a more pronounced strain concentration occurs at the inclusion boundary when the inclusion diameter is larger and the inclusion strength is lower. The crack mode in the infilled red sandstone is independent of the strength of the inclusion. For larger hole diameters, fracture planes form along the compression line, whereas interfacial debonding occurs in red sandstone with smaller hole diameters. Finally, the stress distribution characteristics along the loaded diameter and transverse diameter were analyzed using elastic finite element analyses, which can well explain the cracking mechanism of the infilled disc specimens.

1. Introduction

Rock mass, as a typical geological material, exhibits significant nonlinearity and heterogeneity due to inherent defects or discontinuities in various forms, such as pores, fissures, joints, faults, and shear bands [1–4]. These discontinuities can lead to excessive stress concentrations and uncoordinated deformations in rock masses when subjected to external loads, resulting in crack initiation and propagation along with irreversible damage or even structural

failure of the rock [5–9]. Up to date, numerous studies have been conducted to explore the cracking mechanism of rock or rock-like materials containing preexisting flaws under various compression conditions [10–15]. However, most of these studies focused on artificial flaws with lengths of 15–20 mm and small widths of 1-2 mm, while the presence of macroporosity or open holes that also have detrimental effects on the mechanical properties of rock were rarely considered [16]. It has been observed that rocks such as lithophytic tuff, vesicular basalts [17], and sandstone [18]

commonly contain holes with much larger sizes than the artificially created flaws. The number, shape, size, and distribution of these open defects have been found to significantly influence the mechanical responses of rocks, as demonstrated by experimental and numerical studies [19–23]. To this end, investigations have been carried out to study the fracturing behavior of rock specimens with one or multiple holes under tension or indirect tensile conditions [24–28]. Previous studies primarily focused on the mechanical properties and cracking characteristics of rocks with open flaws or holes, which are crucial for in situ rock engineering applications.

In practical scenarios, however, the fissures or joints within rock masses are often filled with weak interlayers such as clay, sand, and gypsum [29–32]. These inclusions can occur naturally as a result of physical/chemical weathering or joint shearing actions [33] (see Figures 1(a) and 1(b)) or can be manually filled through grouting/shotcreting during the tunnel construction [29, 34–36] (see Figure 1(c)). The fillings in the holes or fissures introduce more complex stress distributions within the rock mass, leading to different failure mechanisms compared to rocks with open flaws [37]. Therefore, investigating the mechanical properties and fracturing evolution of rocks with filled flaws holds great engineering significance.

In this regard, extensive investigations have been conducted on rock specimens with filling materials, as depicted in Figure 2 [38–45]. Under the direct shear conditions, Tian et al. [46] conducted experimental and numerical studies on the shear behavior of cemented concrete-rock joints. Lu et al. [47] investigated the shear deformation and strength behavior of cement-grout-filled joints. Salimian et al. [48] found that grouting positively affected the shear strength of cement-filled joints. In terms of specimens subjected to compression-shear conditions, Butron et al. [49] studied the mechanical behavior of silica sol-grouted hard rocks under unconfined compression and triaxial conditions. Miao et al. [50] performed unconfined compression tests on flawed sandstone specimens, considering factors such as inclination angles and infilling materials (e.g., gypsum, cement, and resin). Du et al. [51] investigated the strength properties and failure patterns of plate-shaped sandstones with two circular inclusions under uniaxial compression. Zhu et al. [39] studied the deformation and cracking processes of sandstones containing various inclusions using digital image correlation (DIC) and acoustic emission (AE) techniques, considering the influences of hole shape on strength and deformation properties. It was observed that inclusions alter crack propagation behaviors and reduce stress concentration intensity at the crack tip zone. However, most existing studies on infilled rock specimens have focused on uniaxial/biaxial compression or shear loading, with limited investigations into the mechanical responses and failure behaviors under tensile loading. To explore the fracturing evolution of specimens under tensile stress, Chang et al. [52] conducted numerical studies on the mechanical behaviors of cement mortar specimens with circular inclusions under diametrical compression. Sharafisafa et al. [33] performed diametrical compression on 3D printed rock-like discs to investigate the effect of infilling materials on the cracking behavior. Nevertheless, the understanding of the deformation and cracking processes of infilled disc specimens under diametrical compression is still not fully elucidated.

In this study, red sandstone and grey sandstone discs with circular inclusions were prepared and submitted to diametrical compression tests. The inclusions had different strengths/stiffness and sizes. The deformation characteristics, mechanical properties, and cracking evolution were systematically explored using SG measurement and the DIC technique. The influences of the inclusion strength and diameter on local strain concentration and cracking behavior were deeply analyzed.

2. Materials and Methodology

2.1. Specimen Preparation.

Two distinct types of sandstones, distinguished by their colors and geological textures, were selected for experimentation in this study. The red sandstones were sourced from Liuyang City, Hunan Province, while the grey sandstones were extracted from an open-pit quarry in Miluo City, Hunan Province. To minimize artificial damage to the rock specimens, both types of sandstones were obtained from the bedrock using mechanical cutting methods. Brazilian discs with dimensions of 50 mm in diameter and 25 mm in thickness were drilled from the rock blocks. A circular hole was then created at the center of each disc specimen. Different hole diameters, including 10 mm, 15 mm, and 20 mm, were considered to investigate the effect of hole size on cracking behaviors. Similar hole diameters were also adopted in previous studies, such as Chang et al. [52] and Wu et al. [22].

To fill the central holes, cement mortars with two different composite ratios were prepared. One composite ratio consisted of cement, sand, and water in a mass ratio of 1: 5.27: 1.16, generating a low-strength cement mortar material (Type I). The other composite ratio consisted of cement, sand, and water in a mass ratio of 1: 3.47: 0.64, resulting in a high-strength cement mortar material (Type II). The specimens were prepared in the same batch to ensure consistent interfacial bonding strength among them. In addition, the infilled specimens were cured under standard temperature and humidity conditions for 28 days. Following these curing conditions, the cement mortar exhibits optimal mechanical performance and forms satisfactory adhesions with the prefabricated hole walls.

To determine the basic mechanical properties of the materials, solid specimens of red sandstone, grey sandstone, Type I cement mortar, and Type II cement mortar were subjected to standard unconfined compression tests and Brazilian disc tests. The stress-strain curves obtained from the unconfined compression tests and the load-displacement curves obtained from the Brazilian disc tests are presented in Figure 3. Table 1 summarizes the basic physical and mechanical parameters of the rocks and cement mortars.

The red sandstone exhibits a P-wave velocity of 2799 m/s, which is 20.8% higher than that of the grey sandstone. Accordingly, the unconfined compressive strength (UCS), Young's modulus, and tensile strength of the red sandstone
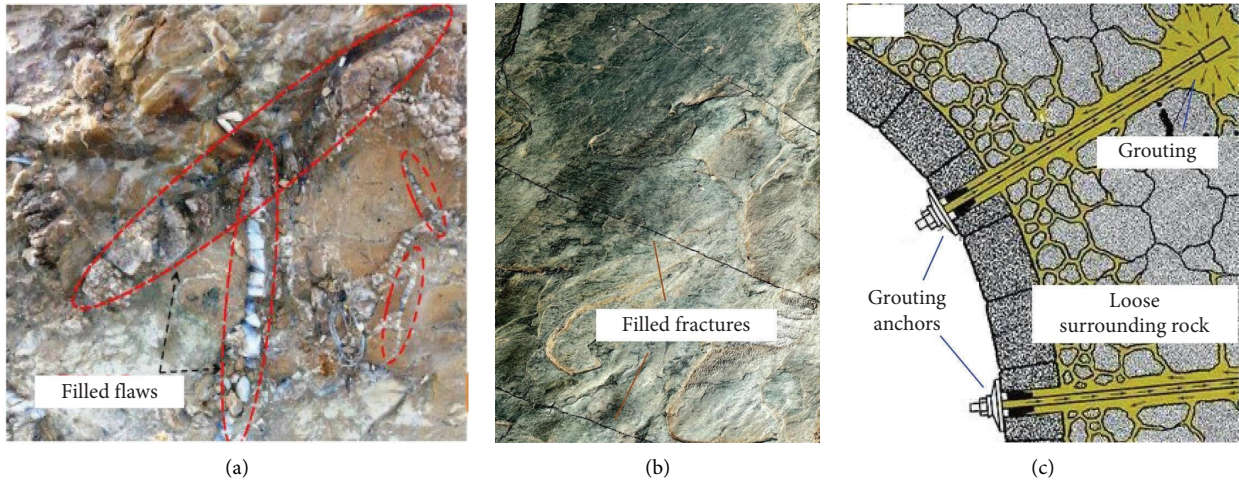
FIGURE 1: In situ filled flaws or fractures (a) jointed rock mass containing filled flaws (after Sharafisafa et al. [33]); (b) rock slope with filled fractures; (c) grouting in the loose surrounding rock.
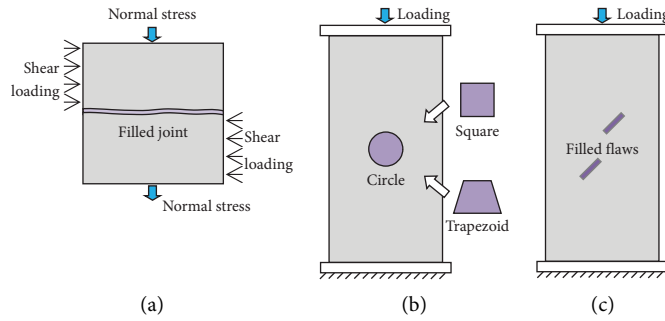

FIGURE 2: Laboratory tests on rocks containing filled joint or flaw: (a) direct shear test on filled rock joint [38]; (b) uniaxial compression test on rocks with varying shapes of inclusion [39]; (c) uniaxial compression test on rocks with filled flaws [40].
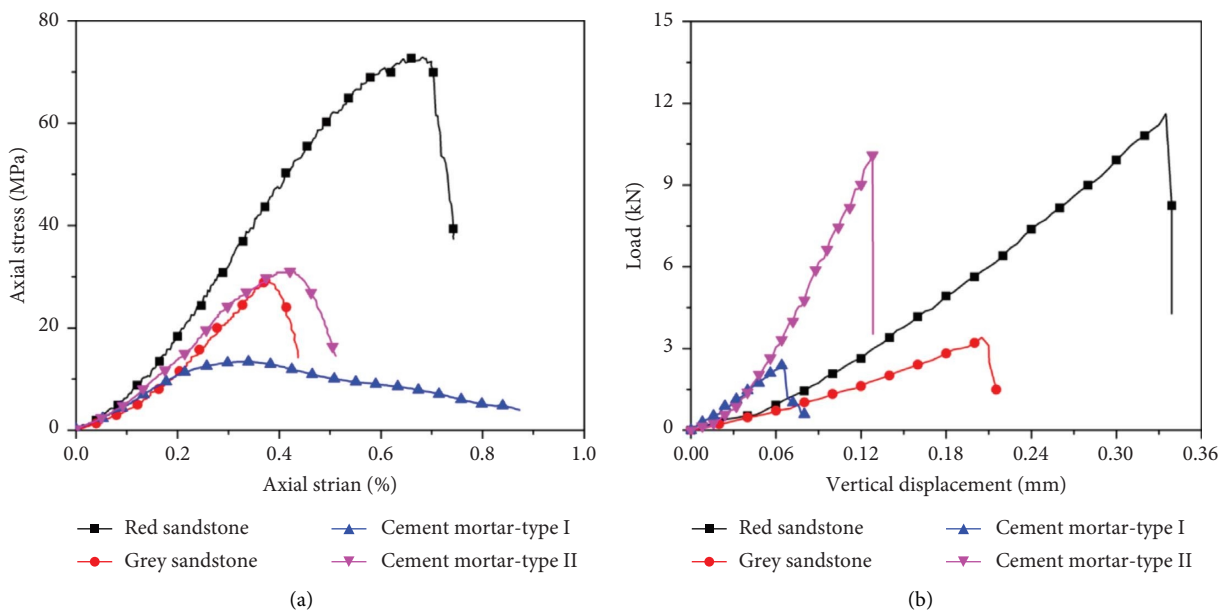

FIGURE 3: Basic mechanical properties of the sandstones and cement mortars: (a) axial stress-strain curves obtained from unconfined compression tests; (b) load-displacement curves obtained from Brazilian disc tests.

TABLE 1: Physical and mechanical properties of the sandstones and cement mortars.

Properties	Red sandstone (ReS)	Grey sandstone (GrS)	Cement mortar-Type I (CM-I)	Cement mortar-Type II (CM-II)
Density (g/cm^3)	2.50	2.33	2.01	2.1
P-wave velocity (m/s)	2799	2317	1906	2240
Poisson's ratio	0.27	0.33	0.22	0.25
Young's modulus (GPa)	15.0	10.6	5.2	10.0
UCS (MPa)	73.2	29.3	13.2	31.6
Tensile strength (MPa)	5.85	1.86	1.31	4.83

Note. The abbreviation names for the materials are shown in parentheses for convenience.

are 2.5 times, 1.4 times, and 3.1 times larger than those of the grey sandstone, respectively, indicating distinct mechanical behaviors between the two types of sandstones. Regarding the cement mortars, CM-II (high-strength cement mortar) demonstrates significantly higher mechanical properties compared to CM-I (low-strength cement mortar). Specifically, the UCS, Young's modulus, and tensile strength of CM-II are 2.4 times, 1.9 times, and 3.7 times larger than those of CM-I, respectively. Furthermore, the P-wave velocity, UCS, and Young's modulus of grey sandstone closely match those of CM-II, as evident from similar stress-strain responses in Figure 3(a), although noticeable discrepancies in Poisson's ratio and tensile strength are observed. The basic physical and mechanical parameters of the four materials differ significantly, which is advantageous for investigating the effect of infilling on the combined specimens. Therefore, four groups of infilled specimens, such as ReS-I, ReS-II, GrS-I, and GrS-II, as shown in Figure 4, were generated. In addition, solid Brazilian disc specimens (BD) and ring-shaped (RS) specimens without infillings were prepared for comparative analysis. Each configuration comprises three specimens, and the averaged parameters obtained from the experiments were used for subsequent analyses.

2.2. Experimental Methodology and Equipment. A hydraulic servo-controlled loading system (Model RMT-150C) was used to conduct the diametrical compression tests. The disc specimens were positioned on the loading platen and compressed diametrically until failure. The loading speed was set to 0.002 mm/s using a displacement control module. This speed ensured that the specimen deformed at a quasi-static strain rate. The applied load was monitored using a small force sensor with a range of 0–20 kN. Strain gauges were attached to the specimen's surface to record the local strains at points of interest during the diametrical compression.

The fracturing process of the specimen under diametrical compression was captured and recorded using a high-speed camera (HS-camera) system. Since the disc specimens were tested under diametrical compression conditions, the total time required to fracture the specimen was approximately 6 minutes, as determined in the preexperiments. Consequently, a lower frame rate was selected to capture and record as many images as possible for subsequent analysis.
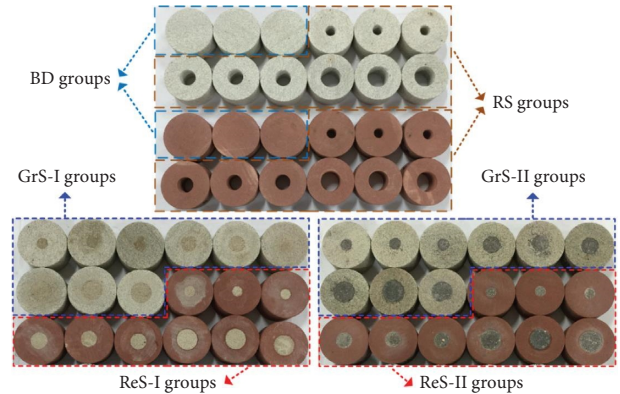

FIGURE 4: Configurations of the specimens.

After calibration, a frame rate of 50 fps was chosen with a resolution of 320×360 pixel array size. These images were then used for digital image correlation (DIC) analysis. A speckle pattern was applied to the specimen's surface to enhance contrast. This was achieved by first spraying white paint to create a white base and then spraying black paint to generate black speckles. Figure 5 illustrates the experimental setup, incorporating the strain gauge measurement and HS-camera system.

3. Results and Analyses

3.1. Load-Displacement Curves. Figures 6 and 7 illustrate the typical vertical load-displacement curves of the red sandstone and grey sandstone specimens with different configurations. It is observed from Figures 6(a) and 7(a) that the load-carrying capacities (i.e., maximum load in the curve) of the ring-shaped ReS specimens and GrS specimens decrease dramatically with increasing inner diameter. When the inner diameter is 10 mm, there is only one force drop observed on the load-displacement curve. Nevertheless, as the inner diameter increases to 15 mm or 20 mm, an additional force drop occurs after the maximum load, indicating that the specimen experiences two fracturing responses to the loading. This phenomenon has been well explained in previous studies [53, 54]. The first fracture occurs at the roof and floor of the inner hole surface due to tensile stress concentration, while the subsequent fracture takes place at
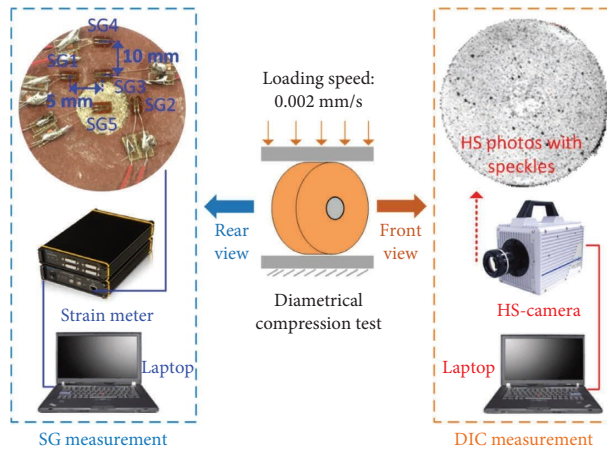
Figure 5: Experimental setup incorporating strain gauge measurement and HS-camera system.
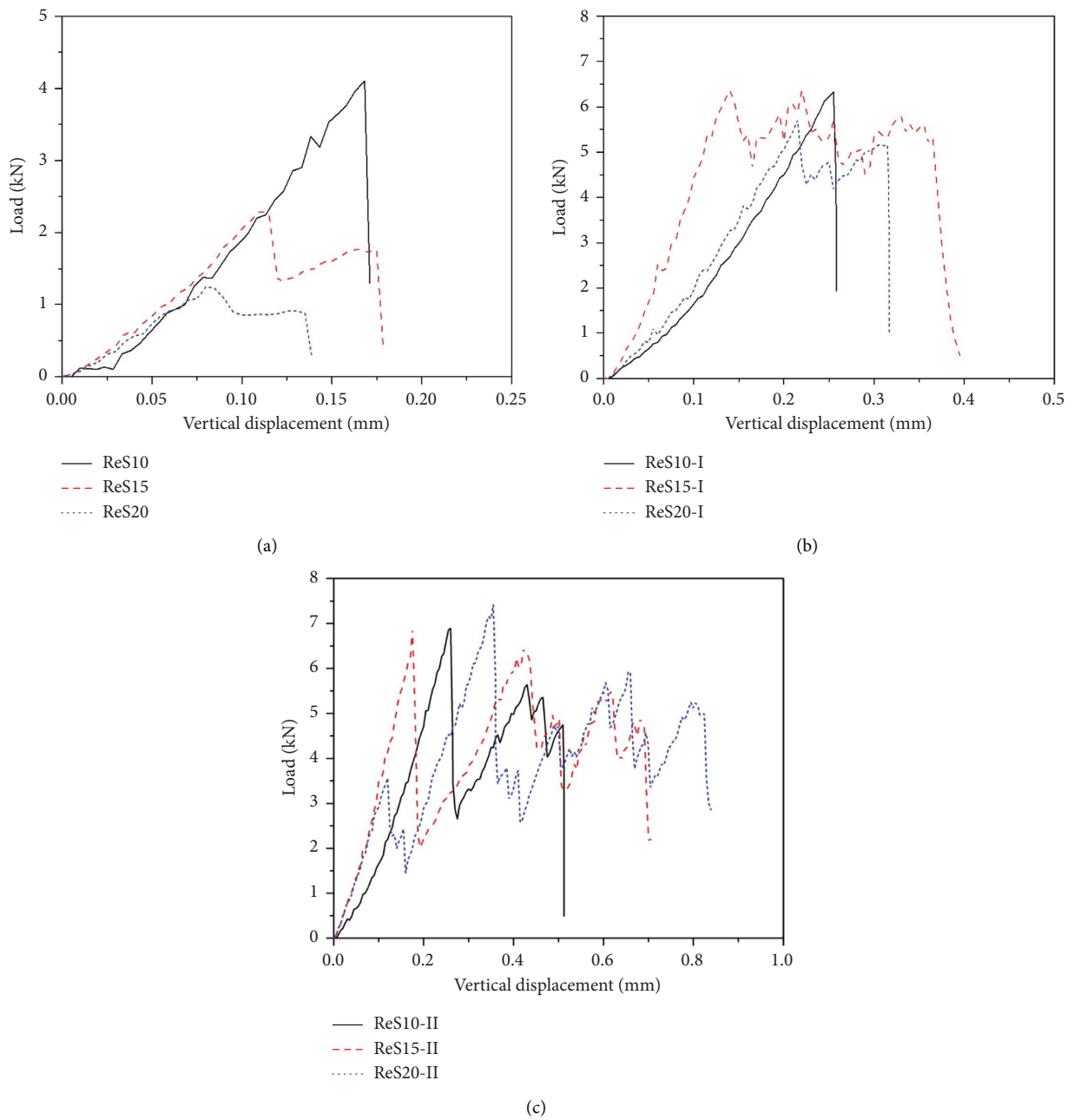

(a)

(b)

(c)

Figure 6: Load-displacement curves of red sandstone specimens (a) without infilling; (b) infilled with CM-I; (c) infilled with CM-II.
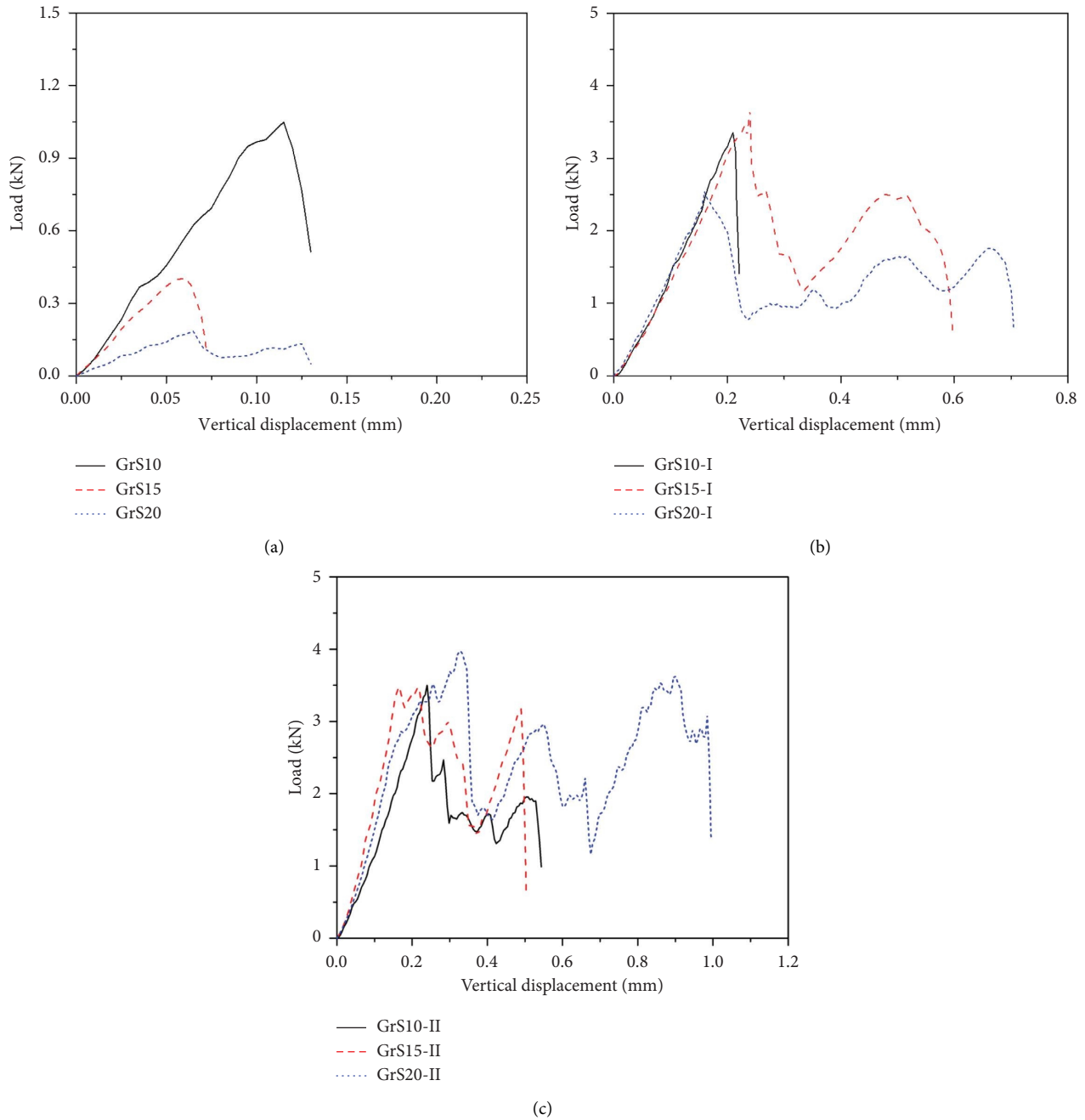
(a)

(b)

(c)

FIGURE 7: Load-displacement curves of grey sandstone specimens (a) without infilling; (b) infilled with CM-I; (c) infilled with CM-II.

the lateral outside surface of the RS specimen in a tensile manner.

On the other hand, when the specimen is infilled, the shape of the load-displacement curve differs significantly from that of the RS specimen. As shown in Figures 6(b), 6(c), 7(b), and 7(c), for the same hole diameter, the infilled specimen exhibits a significantly higher load-carrying capacity compared to the ring-shaped sandstone. Moreover, the infilled specimen displays multiple force drops in the postpeak phase, indicating the occurrence of multiple local failures during the loading process. As illustrated in Section

3.4, these failures were induced not only within the sandstone and cement mortar but also at the interface between the rock and cement mortar.

When comparing specimens infilled with different cement mortars (i.e., low-strength CM-I and high-strength CM-II), it is observed that the specimen infilled with CM-II has much larger vertical deformation and more complex postpeak mechanical behaviors (see Figures 6(c) and 7(c)). This can be attributed to the higher strength and elastic modulus of CM-II compared to CM-I, which provides a more pronounced support effect on the infilled specimen.

In terms of the red sandstone and grey sandstone specimens having the same inclusion material and geometric configuration, it is evident that the red sandstone has a higher load-carrying capacity than the grey sandstone, while the vertical displacement of the red sandstone is smaller than that of the grey sandstone. This phenomenon is largely influenced by the mechanical properties of the rocks, such as the greater strength and Young's modulus of the red sandstone compared to the grey sandstone (refer to Table 1).

3.2. Stiffness and Maximum Peak Load. In this section, the stiffness index is introduced to examine the overall deformation characteristics of the infilled specimens. The stiffness is defined as the ratio of the force to the vertical displacement during the linear phase of the load-displacement curve before the first peak load. Following this definition, Figure 8 presents the relationship between stiffness and hole diameter for the specimens. It is observed that the trends in the stiffness variation with hole diameter are generally similar for both the red sandstone and grey sandstone specimens. Specifically, for the ring-shaped specimens without inclusion, the stiffness decreases monotonically with increasing the hole diameter, manifesting that the hole has a weakening effect on stiffness. Nevertheless, when the specimens are infilled with CM-I or CM-II, the stiffness exhibits a trend of initially increasing and then decreasing as the hole diameter changes from 10 mm to 15 mm and subsequently to 20 mm. The stiffness reaches the highest value when the hole diameter is 15 mm. Furthermore, the stiffness of the ReS15-II and GrS15-II specimens are higher than that of the Brazilian disc specimen, indicating that the high-strength cement mortar provides strong support to the specimens.

As demonstrated in Section 3.1, the infilled specimens exhibit multiple peaks in the load-displacement curves, indicating a progressive cracking process during the loading. In this section, the maximum peak load (MPL) value is selected to further study the relationship between the peak load and hole diameter as well as inclusion material. Figure 9 presents the changes in MPL with respect to the hole diameter for the ReS and GrS specimens with various inclusions. For the RS specimen, the MPL value decreases with increasing hole diameter, similar to the trend observed in stiffness. Under the same hole diameter, the MPL of the infilled specimen is higher than that of the unfilled specimen, indicating an enhancement in the load-carrying capacity due to the inclusion. For instance, the MPL of the GrS20-II specimen is more than 22 times greater than that of the GrS20 specimen without inclusion and 1.5 times greater than that of the GrS20-I specimen. However, the degree of enhancement in load-carrying capacity varies significantly among different configurations. In the case of the GrS specimen infilled with CM-II, the MPL is almost the same as the tensile strength of the solid Brazilian disc. This phenomenon occurs probably due to the similar mechanical properties (e.g., Young's modulus and UCS) of CM-II and the grey sandstone, indicating that the inclusion offsets the weakening effect of the hole, as observed in the RS specimen.

For the ReS-II specimen, the MPL monotonically increases with increasing hole diameter. Nevertheless, for the ReS and GrS specimens with CM-I inclusion, the MPL first increases and then decreases with increasing hole diameter, reaching its highest value when the hole diameter is 15 mm. This phenomenon clearly indicates that the CM-I inclusion material can enhance the load-carrying capacity of both the GrS and ReS specimens. However, the enhancement effect will be negatively compensated when the hole diameter increases. Alternatively, the effective load-carrying capacity of the infilled specimen results from a competitive interplay between the inclusion enhancement and the hole weakening effect.

3.3. Evolutions of Strain Readings. As indicated in Section 3.1, the deformation of the infilled specimen was closely dependent on the inclusion material and hole diameter. In this section, to further study the deformation characteristics of the infilled specimens under diametrical compression, the strain evolution of several locations adjacent to the inclusion-rock interface was examined using strain gauge measurement. The arrangement of the strain gauges is illustrated in Figure 10. SG5 was positioned at the center of the inclusion. SG2 was located at the lateral boundary of the inclusion-rock interface, while SG3 was placed at the roof boundary parallel to the compression line. SG1 was placed on the left side of SG3 and was 5 mm away from SG3. SG4 was located 10 mm away from SG3 along the compression diameter. SG1 was used to record the strain evolution of the point of interest that is not in the loading line.

Figure 11 illustrates the strain evolutions recorded by the SGs on the infilled ReS specimens with various hole diameters and inclusions. The time-to-fracture line indicates when the specimen loses partial or entire load-carrying capacity. Positive values in the SG readings represent tensile strain, while negative values represent compressive strain. It can be seen that irrespective of the inclusion material or hole diameter, the tensile strain in the SG3 reading is consistently higher than that in the SG4 reading, indicating a change in the tensile strain distribution in the specimen due to the presence of the inclusion. In addition, the tensile strain concentration occurs at SG3 due to the hole effect, even when the hole is infilled with cement mortar. Furthermore, when comparing Figure 11(a) with Figure 11(b) and Figure 11(c) with Figure 11(d), it is found that the SG3 reading increases significantly with increasing hole diameter, indicating a more pronounced intensity of tensile strain concentration in cases with a larger hole diameter. The SG1 reading remains positive before failure in all test scenarios and increases with increasing loading time. Nevertheless, the SG1 reading is considerably lower than the SG3 reading, demonstrating that the highest tensile strain occurs at the inclusion boundary. This observation is further supported by the smaller SG5 reading compared to the SG3 reading. Furthermore, the SG2 reading remains consistently negative throughout the entire cracking process, demonstrating that the lateral boundary of the inclusion remains in a state of compression. These results indicate that although
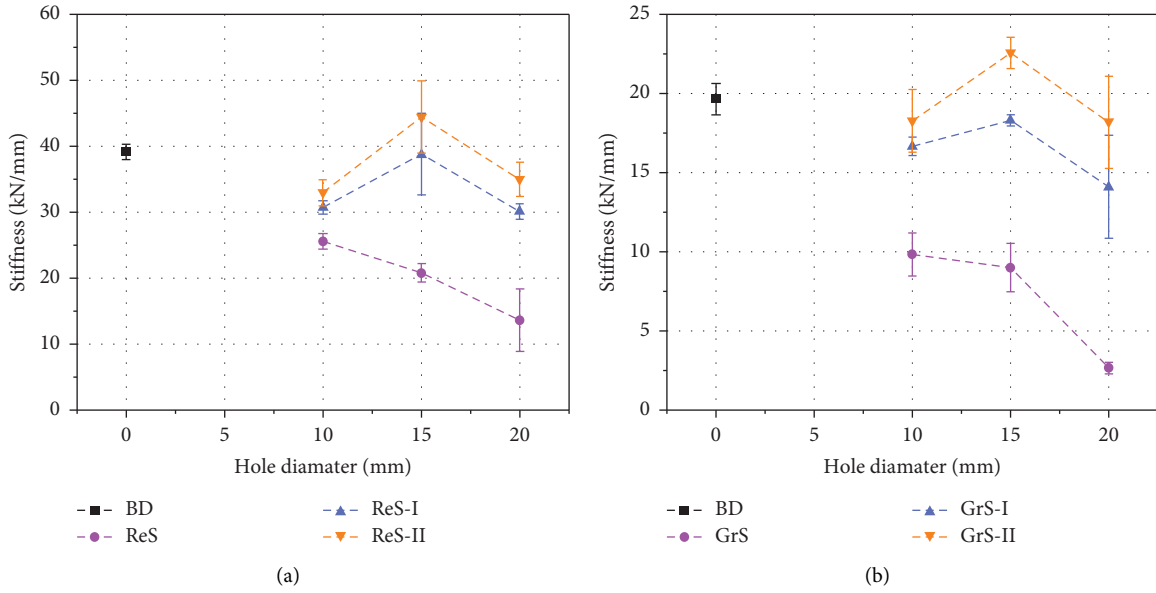
FIGURE 8: Variations in the stiffness of specimens with different inclusion scenarios: (a) red sandstone; (b) grey sandstone.
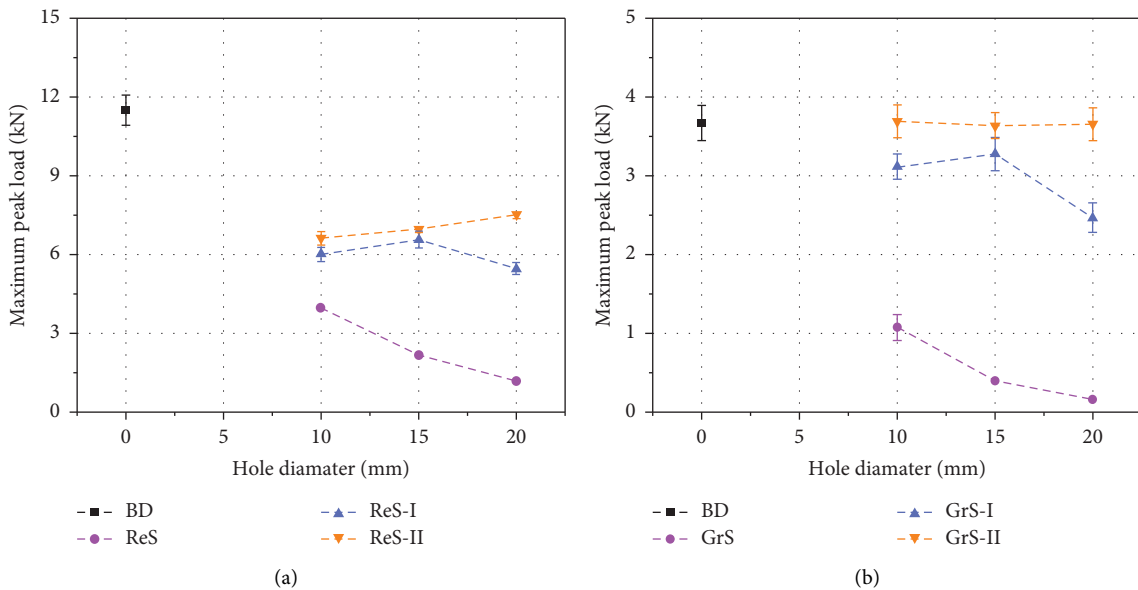

FIGURE 9: Variations in the MPL of specimens with different inclusion scenarios: (a) red sandstone; (b) grey sandstone.

the central hole is filled with CM-I or CM-II, tensile strain concentration still occurs at the roof boundary of the inclusion along the compression line. Similar tensile regions have been observed in ring-shaped rock specimens, as shown in Li et al. [55]. The mismatch in the deformation compatibility at the inclusion boundary may be a contributing factor to the initiation of interfacial cracking, which will be further explained in the subsequent sections.

Figure 12 shows the strain evolutions recorded by the strain gauges on the infilled GrS specimens. It is seen that, the variations in the strain values obtained by the strain gauge for the infilled GrS specimens are similar to those of the infilled ReS specimens. The main difference lies in their

responses to load drops in the load-time curves. For example, in the case of the GrS20-II specimen (Figure 12(d)), multiple load peaks occur during the diametrical compression process, leading to fluctuations in the strain readings of SG3 and SG4 that correspond to the load drops.

To further investigate the effects of the inclusion and hole diameter on the deformation features, Figure 13 summarizes the changes in the SG1 and SG3 readings at the MPL point for the infilled ReS and GrS specimens. It can be seen that, for all the ReS and GrS specimens, the values of SG1 and SG3 increase with increasing hole diameter, irrespective of the inclusion material types. This phenomenon aligns with previous experimental and numerical findings [30, 52].
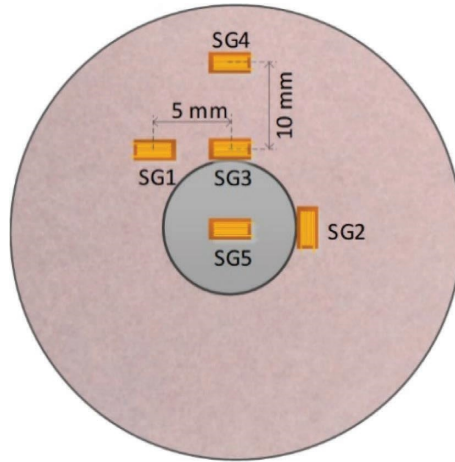
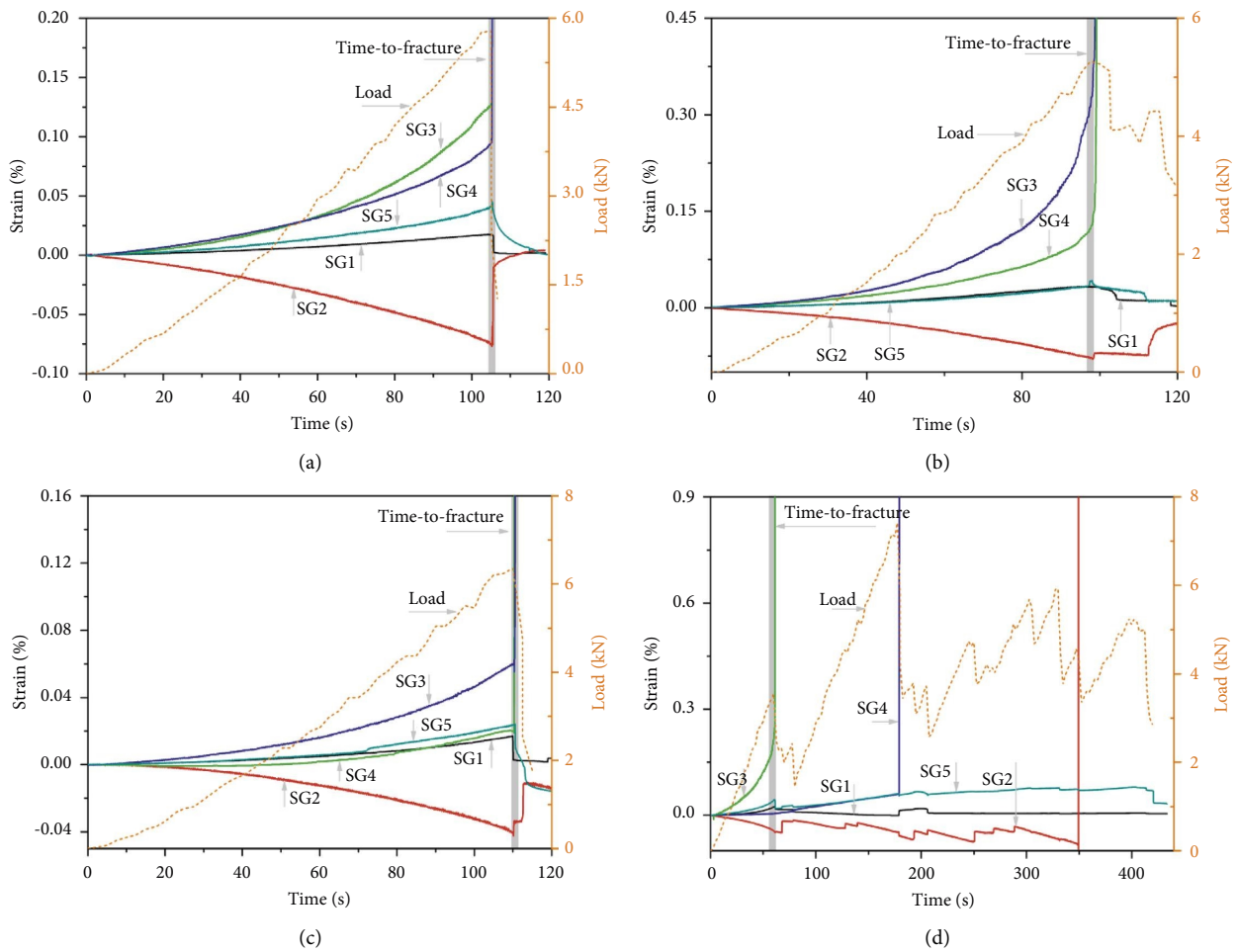FIGURE 10: Arrangement of the strain gauges.

(a)

(b)

(c)

(d)

FIGURE 11: Strain evolutions of the infilled ReS specimens: (a) ReS10-I; (b) ReS20-I; (c) ReS10-II; (d) ReS20-II.

Furthermore, for cases with the same hole diameter, specimens with low-strength inclusion (CM-I) exhibit higher SG1 and SG3 readings compared to specimens with high-strength inclusion (CM-II). However, it is worth noting that

the ring-shaped specimens without inclusion demonstrate the highest SG1 and SG3 readings, as shown in Figure 13. These results show that a more intensive strain concentration area is generated at the inclusion boundary when the
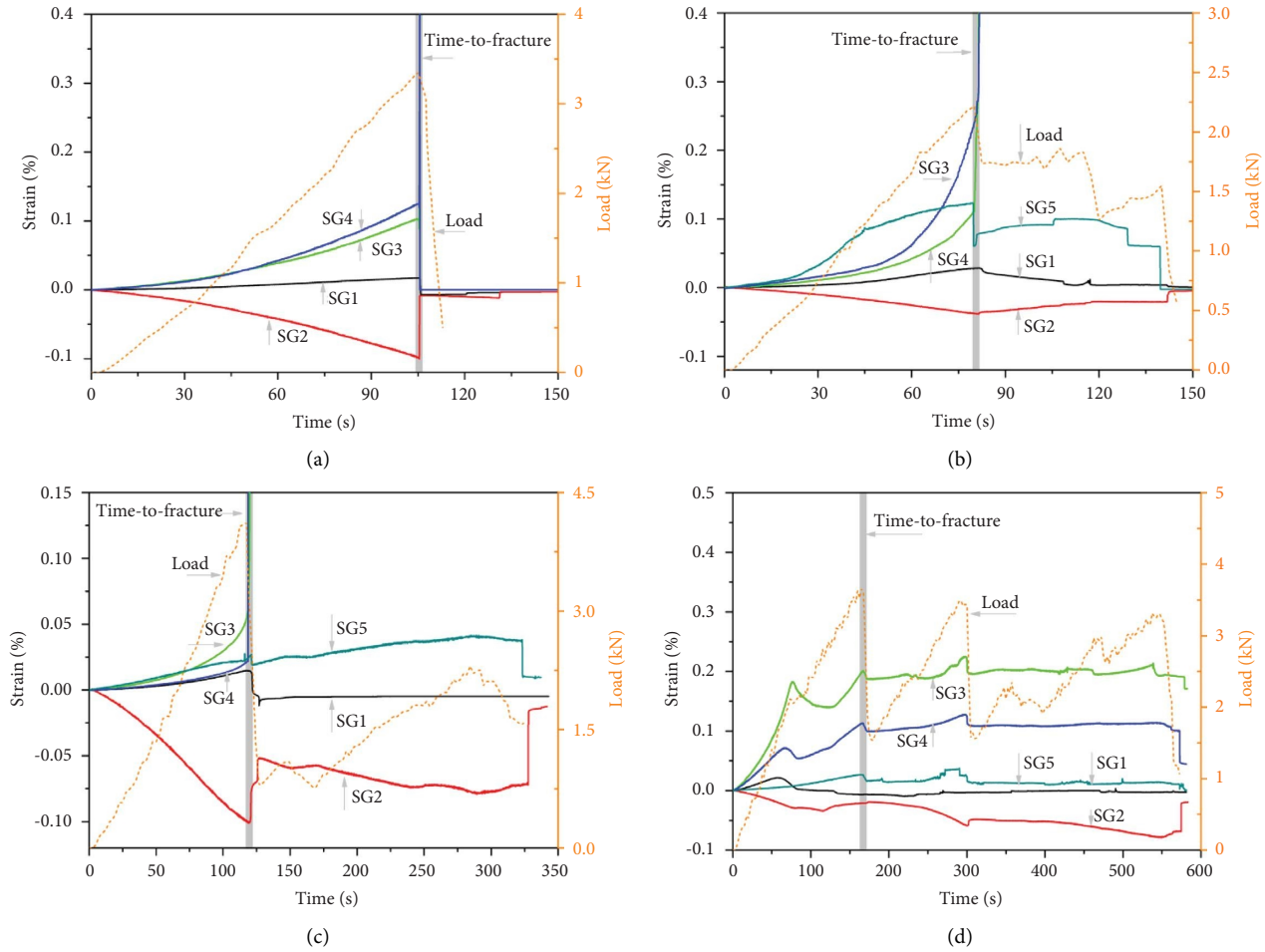
FIGURE 12: Strain evolutions of the infilled GrS specimens: (a) GrS10-I; (b) GrS20-I; (c) GrS10-II; (d) GrS20-II.

hole diameter is larger and the inclusion material has lower strength. Consequently, when the hole diameter is the same, the RS specimen without inclusion exhibits the lowest load-carrying capacity, followed by the CM-I filled specimen and then the CM-II filled specimen (Figure 9).

3.4. Crack Evolution Process from the DIC Measurement. The images photographed by the HS-camera during the loading process were used to calculate the distribution of the maximum principal strain. Through visual inspections of the specimen surface and statistical analyses of the strain distributions, it was observed that macrocracking occurs when the maximum principal strain exceeds 3.5%. Therefore, areas with a maximum principal strain exceeding 3.5% are considered as locations where macrofracture initiates. To better demonstrate the cracking process, the maximum principal strain contour was limited to the range of 0–3.5%.

Figure 14 presents the cracking process of red sandstone specimens with varying hole diameters and inclusions. It can be observed that specimens with identical hole diameters but different inclusion materials exhibit similar crack modes. For example, regardless of whether the inclusion is CM-I or CM-II, the inclusions in the ReS10-I and ReS10-II specimens

remain intact (Figures 14(a) and 14(b)), although debonding failure occurs at the inclusion-rock interface. The specimens with a 20 mm hole diameter (Figures 14(c) and 14(d)) were split into two halves along the loaded diameter. This phenomenon demonstrates that the crack mode of red sandstone appears to be independent of the strength of the inclusion. This is likely due to the significant disparity between the strength of the red sandstone and the inclusion (i.e., the strength of the red sandstone is 2.3 times greater than that of the high-strength inclusion and 5.5 times for the low-strength inclusion), which minimizes the influence of the inclusion's strength on the cracking behavior. However, as mentioned above, when the inclusion material is the same, significant differences in crack mode are observed for different hole diameters. For example, with a larger hole diameter of 20 mm, the fracture plane occurs along the compression line. Nevertheless, specimens with a smaller hole diameter of 10 mm tend to lose their load-carrying capacity due to interfacial debonding.

Figure 15 illustrates the cracking process of the grey sandstone specimens with varying inner diameters and inclusions. The cracking behaviors of grey sandstone differ significantly from those of red sandstone. In the case of grey sandstone with a 10 mm hole diameter, the
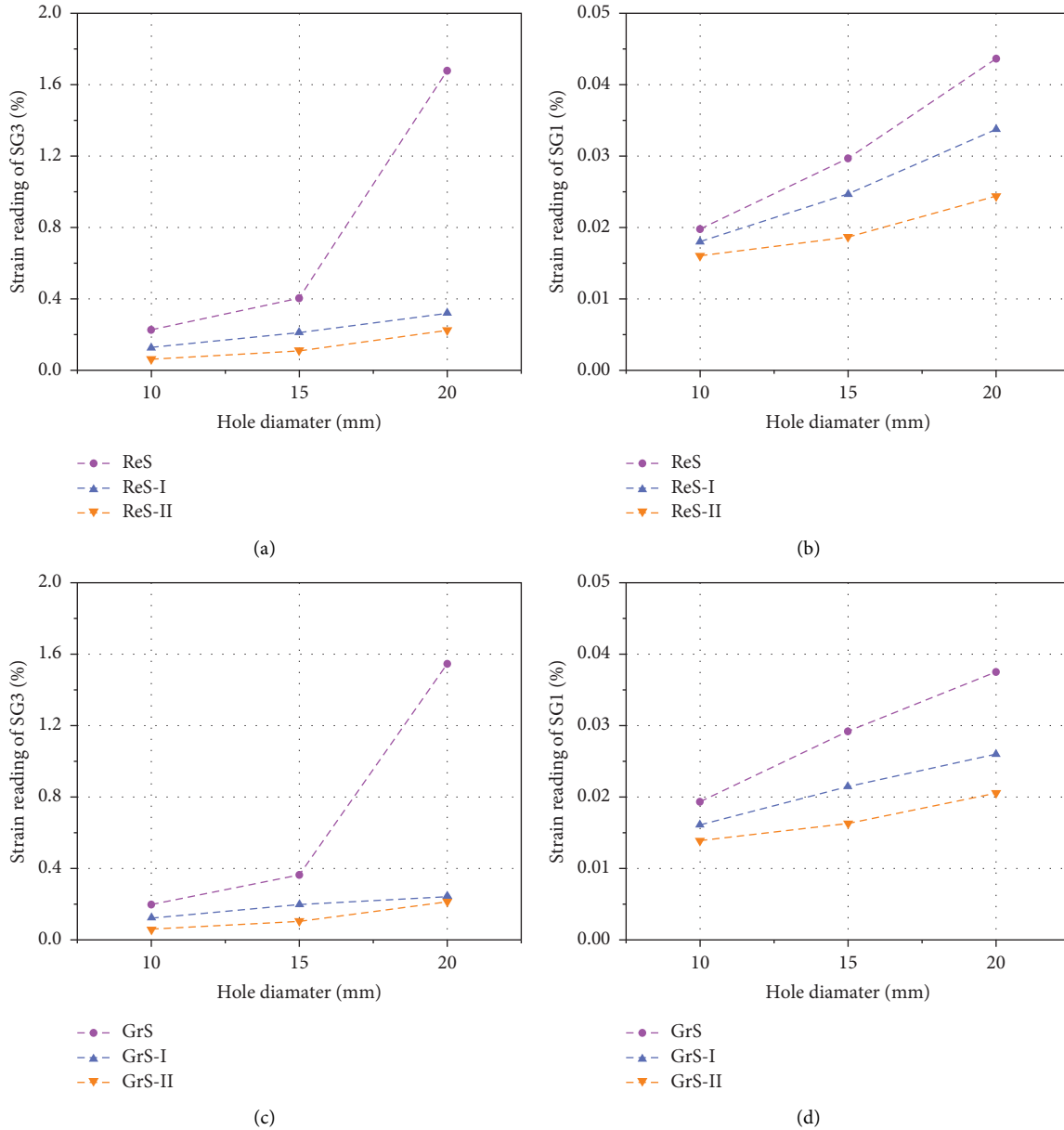
FIGURE 13: Variations in the SG1 and SG3 readings at the MPL point for the specimens with different geometric configurations: (a) SG3 reading of the red sandstone; (b) SG1 reading of the red sandstone; (c) SG3 reading of the grey sandstone; (d) SG1 reading of the grey sandstone.

final fracture plane generally passes through the inclusion, but it does not align with the center compression line (Figures 15(a) and 15(b)). Comparing these results with Figures 14(a) and 14(b), it can be observed that when the hole diameter is small, the growth of the fracture plane is significantly influenced by the hole size effect, making the fracture more prone to propagate towards the inclusion-rock interface. However, this crack mode is markedly different from that of the grey sandstone with a 20 mm inner diameter (Figures 15(c) and 15(d)), where failure is primarily induced by interfacial debonding. The cracking process of infilled sandstone is closely related to

the hole diameters and inclusions, as explained in Section 3.2.

Based on the aforementioned illustrations, three types of failure can be observed in infilled specimens: interfacial debonding, tensile splitting in the sandstone, and tensile splitting in the inclusion. Interfacial debonding initially occurs at either the left or right side of the interface due to a deformation mismatch. Subsequently, tensile cracking is initiated at the crown and floor of the hole as a result of compression. With further increases in the diametrical load, splitting failures in the sandstone and inclusion become evident.
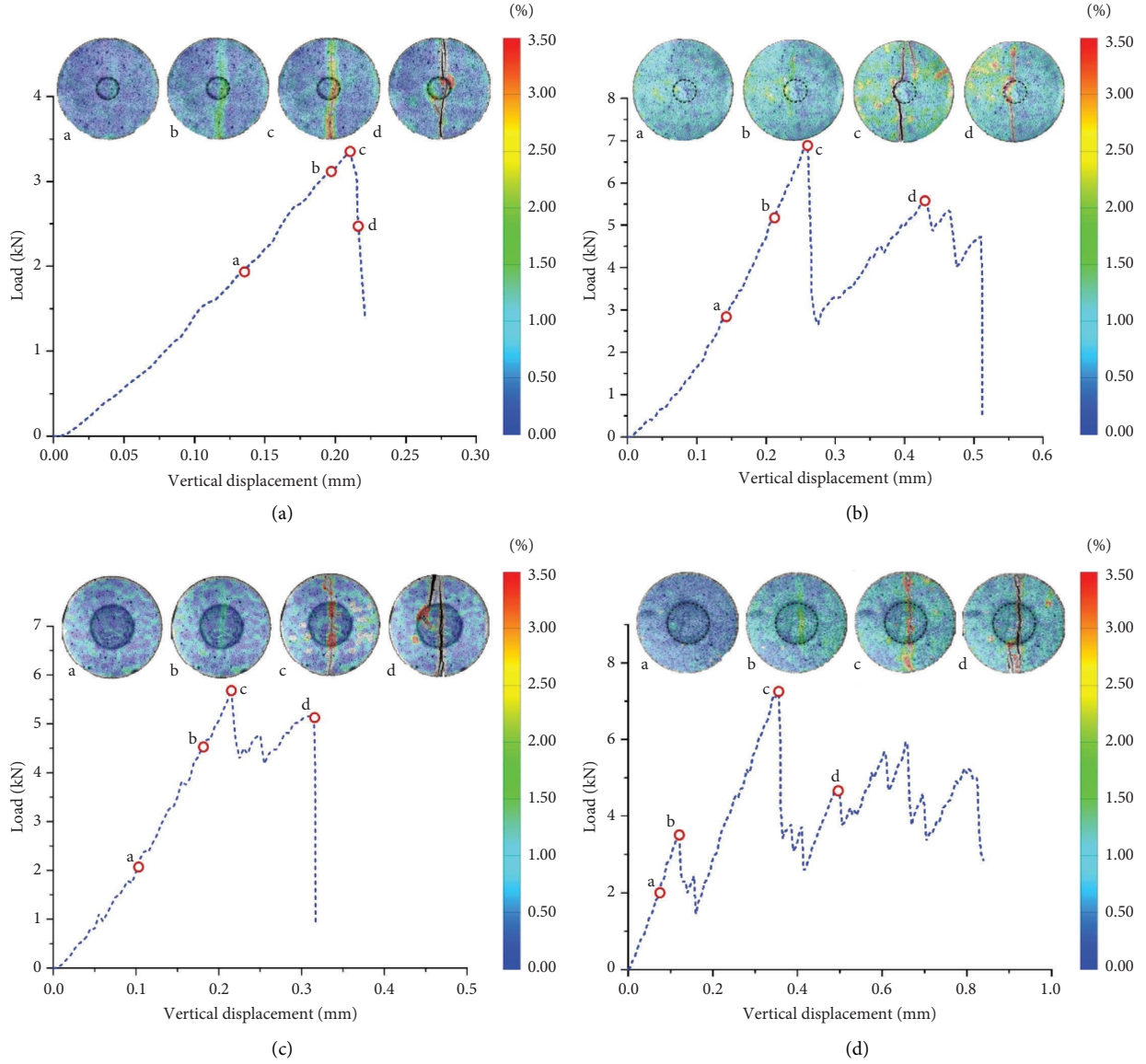
(a)

(b)

(c)

(d)

Figure 14: Cracking process of the red sandstone specimens under diametrical compression: (a) ReS10-I; (b) ReS10-II; (c) ReS20-I; (d) ReS20-II.

4. Discussion

From the above analyses, it is found that the presence of inclusion leads to nonuniform stress distribution and un-coordinated deformation at the inclusion-rock interface during diametrical compression. This ultimately results in various types of failures, as depicted in Figures 14 and 15. The stress field of a homogeneous disc under diametrical compression has been thoroughly discussed in previous studies [56, 57]. Based on the linear elasticity theory, the analytical solution for a homogeneous Brazilian disc under diametrical compression can be expressed as follows [58, 59]:

$$
\left\{
\begin{aligned}
\sigma_x &= -\frac{2P}{\pi t}\left[\frac{x^2(R-y)}{\left((R-y)^2+x^2\right)^2}+\frac{x^2(R+y)}{\left((R+y)^2+x^2\right)^2}-\frac{1}{2R}\right], \\
\sigma_y &= -\frac{2P}{\pi t}\left[\frac{(R-y)^3}{\left((R-y)^2+x^2\right)^2}+\frac{(R+y)^3}{\left((R+y)^2+x^2\right)^2}-\frac{1}{2R}\right], \\
\tau_{xy} &= -\frac{2P}{\pi t}\left[\frac{x(R-y)^3}{\left((R-y)^2+x^2\right)^2}+\frac{x(R+y)^3}{\left((R+y)^2+x^2\right)^2}\right].
\end{aligned}
\right.
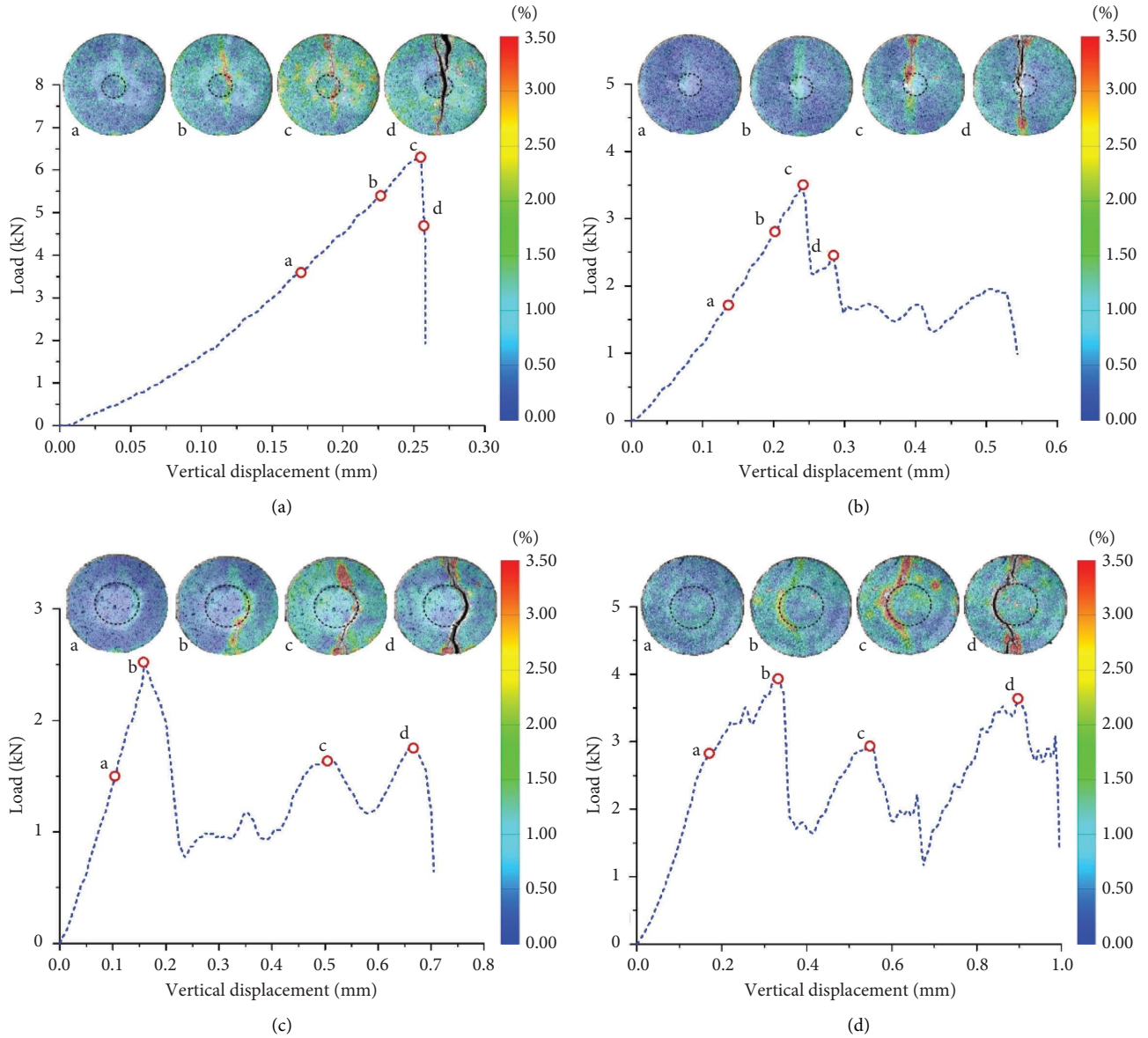$$

(1)

(a)

(b)

(c)

(d)

FIGURE 15: Cracking process of the grey sandstone specimens under diametrical compression: (a) GrS10-I; (b) GrS10-II; (c) GrS20-I; (d) GrS20-II.

where P is the applied load, R is the disc radius, and t is the disc thickness. Equation (1) suggests that along the compression line ($x = 0$), the horizontal stress σ_x exhibits tensile behavior and equals a constant value of $P/(\pi Rt)$. This value can be used to determine the tensile strength of the homogeneous disc when P reaches its maximum. Along the transverse diameter line ($y = 0$), the vertical stress σ_y is compressive, and the maximum value occurs in the center of the disc.

In this study, the Brazilian disc specimens are not homogeneous but are instead infilled with different inclusions. Deriving a closed-form solution for the stress distribution in the infilled disc is challenging. Therefore, finite element (FE) analyses were conducted to explore the stress distribution in the sandstone, inclusion, and the rock-inclusion interface. Figure 16 presents the numerical model with the loading and

boundary conditions. A quarter model was used to reduce computation time. Based on the experimental findings in Section 3, it was observed that failures primarily occur along the vertical diameter or at the rock-inclusion interface. Hence, it was crucial to examine the stress distributions along the loaded diameter and the transverse diameter, particularly the rock-inclusion interface to illuminate the cracking mechanism. To facilitate comparison, the stresses derived from the numerical simulation were normalized by the equivalent tensile stress ($P/(\pi Rt)$).

Figure 17 presents the normalized Y-stress distribution along the X-axis and the normalized X-stress distribution along the Y-axis. The analytical solution and FE solution for the homogeneous Brazilian disc are also included for comparison. Positive stress values denote tensile stress, while negative stress values denote compressive stress. It is evident
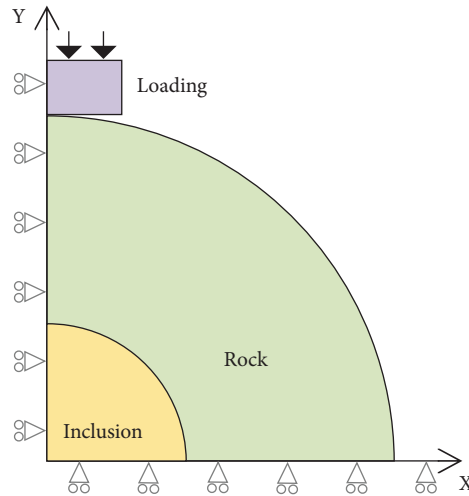
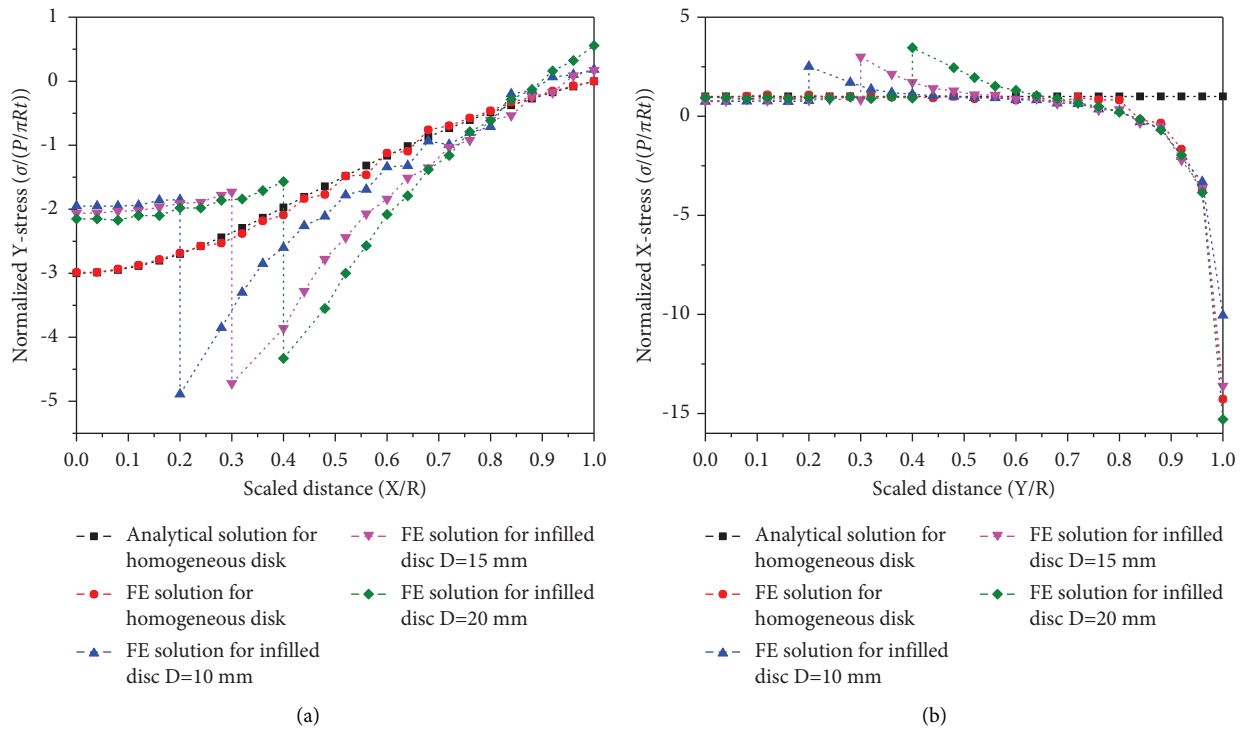FIGURE 16: FE model with loading and boundary conditions.

(a)

(b)

FIGURE 17: FE results of the infilled disc under diameter compression: (a) normalized Y-stress along the X-axis vs. scaled distance; (b) normalized X-stress along the Y-axis vs. scaled distance.

from Figure 17(a) that the center of the infilled disc experiences a compression state, but the magnitude is considerably smaller than that of the homogeneous disc. At the rock-inclusion interface, the compressive stress dramatically increases, leading to a concentrated stress zone. However, the extent of stress concentration diminishes with increasing inclusion diameter. Since the numerical results in Figure 17 are based on the properties of red sandstone, the rock-inclusion interface of the 10 mm infilled disc exhibits a higher stress concentration compared to that of the 20 mm infilled disc. Consequently, the 10 mm infilled disc is more

prone to fracture at the interface, as observed in Figure 14, where debonding failure occurs. In contrast, as shown in Figure 18(b), the X-stress (in tensile behavior) exhibits a substantial increase at the interface between the inclusion and rock, with the magnitude escalating as the inclusion diameter increases. The numerical results verify that higher tensile stress occurs along the compression line for discs with larger inclusion diameters, making them more susceptible to splitting along the loaded diameter. This mechanism also explains the splitting of red sandstone discs with a 20 mm inclusion diameter, as depicted in Figure 14.
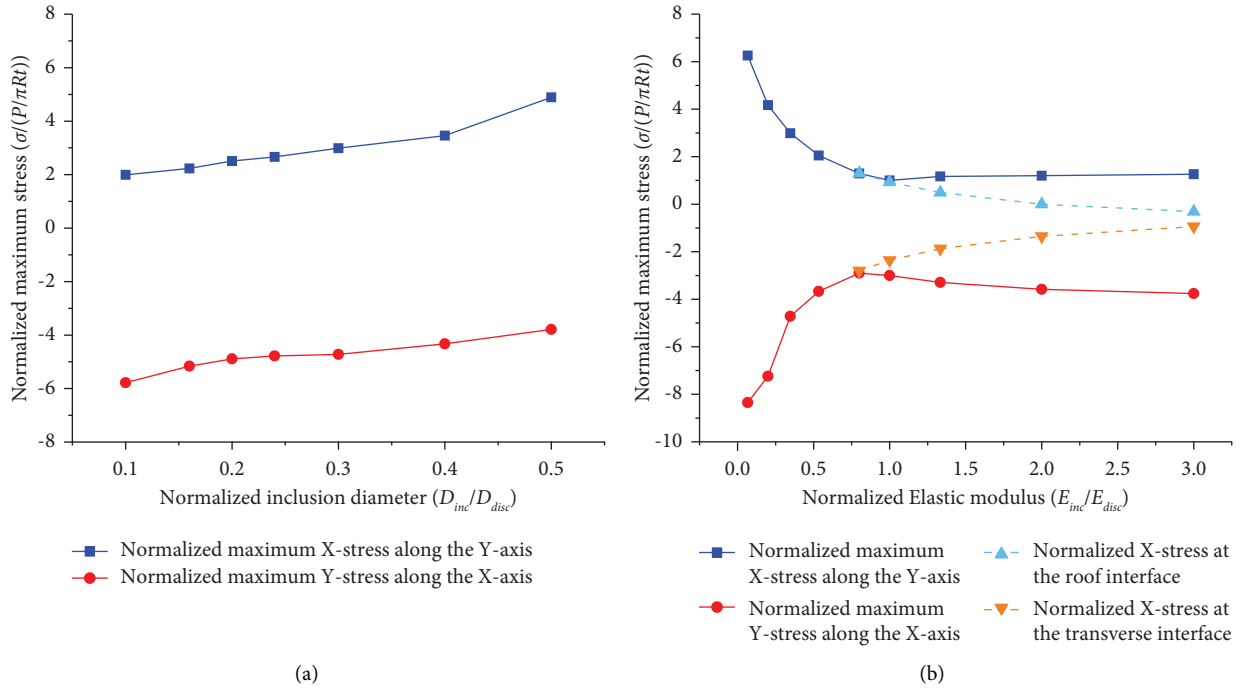
FIGURE 18: (a) Relationship between normalized maximum stress and D_{inc}/D_{disc}; (b) relationship between normalized maximum stress and E_{inc}/E_{disc}.

It should be noted that the failure mechanism of the infilled disc under diametrical compression is complex and influenced by various factors, such as the mechanical properties of the rock, the mechanical properties of the inclusion, and the inclusion diameter. To further explore these relationships, additional FE modeling studies were conducted. The inclusion diameter varied from 5 mm to 25 mm, and the elastic modulus of the inclusion varied from 1 GPa to 45 GPa. Figure 18 illustrates the relationships between the normalized maximum stress and the normalized inclusion diameter (D_{inc}/D_{disc}) and the normalized inclusion elastic modulus (E_{inc}/E_{disc}). It is observed that as the inclusion diameter increases, the normalized maximum X-stress along the loaded diameter monotonically increases, while the compressive stress concentration at the transverse interface weakens. This phenomenon is consistent with the observations in Figure 17. However, as shown in Figure 18(b), with increasing the normalized elastic modulus, the normalized maximum stresses initially decrease and then increase. Specifically, when E_{inc}/E_{disc} is less than 1.0, the maximum stress concentration intensity decreases with increasing the normalized elastic modulus. Nevertheless, when E_{inc}/E_{disc} is larger than 1.0, the maximum stress concentration intensity (either tensile or compressive) increases with increasing normalized elastic modulus. Moreover, the location of the maximum stress shifts from the inclusion-rock interface to the center of the inclusion when E_{inc}/E_{disc} exceeds 1.0 (see Figure 18(b)). It is important to highlight that the FE analyses presented here were based on the elastic deformation of the infilled disc. However, under diametrical compression, the deformation and cracking characteristics are also influenced by the bonding

strength at the interface. The failure of the infilled disc is a competing result of tensile limit, compressive limit, and bonding strength, which should be further, investigated in future studies, including the elastoplastic and postpeak deformations of the infilled disc subjected to diametrical compression.

5. Conclusions

Red sandstone and grey sandstone disc specimens, filled with inclusions of different strengths and diameters, were prepared for diametrical compression tests. The local strain concentration intensity and cracking process at the interface between the rock and inclusions were studied using the SG and DIC measurement techniques. The stress distribution along the loaded diameter and transverse diameter was analyzed using the elastic finite element method. The findings from the study lead to the following conclusions:

(1) The presence of the inclusion introduces more complex deformation and cracking behaviors in the infilled sandstones. The sandstone infilled with CM-II exhibits significantly larger vertical deformation and more intricate postpeak mechanical behaviors in comparison to the sandstone with CM-I inclusion.

(2) The MPL of the red sandstone infilled with CM-II increases continuously as the inclusion diameter decreases. However, the MPL of the grey sandstone infilled with CM-II remains approximately constant regardless of the hole diameter. The effective load-carrying capacity of the infilled sandstone was

determined by the competing effects of inclusion enhancement and hole weakening.

(3) When the inclusion diameter is larger and the inclusion strength is lower, a more pronounced strain concentration occurs at the inclusion boundary. The crack mode in the infilled red sandstone is independent of the inclusion strength. In cases where the hole diameter is larger, the fracture planes form along the compression line, while interfacial debonding occurs in the red sandstone with a smaller hole diameter.

Data Availability

The data used to support the findings of this study are available from the corresponding author upon request.

Conflicts of Interest

The authors declare that they have no conflicts of interest.

Acknowledgments

References

[1] L. Weng, L. Q. Huang, A. Taheri, and X. B. Li, "Rockburst characteristics and numerical simulation based on a strain energy density index: a case study of a roadway in Linglong gold mine, China," *Tunnelling and Underground Space Technology*, vol. 69, pp. 223–232, 2017.

[2] Q. H. Wu, L. Weng, Y. L. Zhao, and F. Feng, "Influence of infilling stiffness on mechanical and fracturing responses of hollow cylindrical sandstone under uniaxial compression tests," *Journal of Central South University*, vol. 28, pp. 2485–2498, 2021.

[3] L. Weng, Z. J. Wu, S. L. Zhang, Q. S. Liu, and Z. F. Chu, "Real-time characterization of the grouting diffusion process in fractured sandstone based on the low-field nuclear magnetic resonance technique," *International Journal of Rock Mechanics and Mining Sciences*, vol. 152, 2022.

[4] S. S. Yu, W. C. Zhu, and L. L. Niu, "Experimental and numerical evaluation on debonding of fully grouted rockbolt under pull-out loading," *International Journal of Coal Science & Technology*, vol. 9, 2022.

[5] M.-D. Wei, F. Dai, N.-W. Xu, T. Zhao, and Y. Liu, "An experimental and theoretical assessment of semi-circular bend specimens with chevron and straight-through notches for mode I fracture toughness testing of rocks," *International Journal of Rock Mechanics and Mining Sciences*, vol. 99, pp. 28–38, 2017.

[6] L. Weng, X. Li, A. Taheri, Q. Wu, and X. Xie, "Fracture evolution around a cavity in brittle rock under uniaxial compression and coupled static–dynamic loads," *Rock Mechanics & Rock Engineering*, vol. 51, 2018.

[7] P. Feng, M. Wei, F. Dai, R. Tang, H. Qiu, and J. Gong, "DEM investigation on the mechanical behaviors of flawed specimens subjected to coupled static-dynamic loads," *Soil Dynamics and Earthquake Engineering*, vol. 135, Article ID 106220, 2020.

[8] P. Feng, Y. Xu, and F. Dai, "Effects of dynamic strain rate on the energy dissipation and fragment characteristics of cross-fissured rocks," *International Journal of Rock Mechanics and Mining Sciences*, vol. 138, Article ID 104600, 2021.

[9] L. Weng, Z. J. Wu, Z. Y. Wang, Z. F. Chu, X. Y. Xu, and Q. S. Liu, "Acoustic emission source localization in heterogeneous rocks with random inclusions using a PRM-based wave velocity model," *Rock Mechanics and Rock Engineering*, vol. 56, pp. 3301–3315, 2023.

[10] A. Bobet and H. H. Einstein, "Numerical modeling of fracture coalescence in a model rock material," *International Journal of Fracture*, vol. 92, p. 221, 1998.

[11] C. H. Park and A. Bobet, "Crack coalescence in specimens with open and closed flaws: a comparison," *International Journal of Rock Mechanics and Mining Sciences*, vol. 46, pp. 819–829, 2009.

[12] M. Sagong, D. Park, J. Yoo, and J. S. Lee, "Experimental and numerical analyses of an opening in a jointed rock mass under biaxial compression," *International Journal of Rock Mechanics and Mining Sciences*, vol. 48, pp. 1055–1067, 2011.

[13] S. Q. Yang, T. Xu, L. He, H. W. Jing, S. Wen, and Q. L. Yu, "Numerical study on failure behavior of brittle rock specimen containing pre-existing combined flaws under different confining pressure," *Archives of Civil and Mechanical Engineering*, vol. 15, pp. 1085–1097, 2015.

[14] C. T. Zhou, H. P. Xie, J. B. Zhu, Z. H. Wang, C. B. Li, and F. Wang, "Mechanical and fracture behaviors of brittle material with a circular inclusion: insight from infilling composition," *Rock Mechanics and Rock Engineering*, vol. 55, pp. 3331–3352, 2022.

[15] A. Staniek, "Technical problems and non destructive testing of rock bolt support systems in mines," *International Journal of Coal Science & Technology*, vol. 10, 2023.

[16] C. Jespersen, M. MacLaughlin, and N. Hudyma, "Strength, deformation modulus and failure modes of cubic analog specimens representing macroporous rock," *International Journal of Rock Mechanics and Mining Sciences*, vol. 47, pp. 1349–1356, 2010.

[17] V. Palchik, "Influence of porosity and elastic modulus on uniaxial compressive strength in soft brittle porous sandstones," *Rock Mechanics and Rock Engineering*, vol. 32, pp. 303–309, 1999.

[18] A. A. Al-Harthi, R. M. Al-Amri, and W. M. Shehata, "The porosity and engineering properties of vesicular basalt in Saudi Arabia," *Engineering Geology*, vol. 54, pp. 313–320, 1999.

[19] Z. Zhou, L. Tan, W. Cao, Z. Zhou, and X. Cai, "Fracture evolution and failure behaviour of marble specimens containing rectangular cavities under uniaxial loading," *Engineering Fracture Mechanics*, vol. 184, pp. 183–201, 2017.

[20] W. Zeng, S.-Q. Yang, and W.-L. Tian, "Experimental and numerical investigation of brittle sandstone specimens containing different shapes of holes under uniaxial compression," *Engineering Fracture Mechanics*, vol. 200, pp. 430–450, 2018.

[21] M. Tao, Z. Li, W. Cao, X. Li, and C. Wu, "Stress redistribution of dynamic loading incident with arbitrary waveform through a circular cavity," *International Journal for Numerical and Analytical Methods in Geomechanics*, vol. 43, pp. 1279–1299, 2019.

[22] H. Wu, Y. Ju, X. Han et al., "Size effects in the uniaxial compressive properties of 3D printed models of rocks: an experimental investigation," *International Journal of Coal Science & Technology*, vol. 9, 2022.

[23] L. Zhou, W. T. Gao, L. Y. Yu, Z. M. Zhu, J. X. Chen, and X. K. Wang, "Thermal effects on fracture toughness of cracked straight-through Brazilian disk green sandstone and granite," *Journal of Rock Mechanics and Geotechnical Engineering*, vol. 14, pp. 1447–1460, 2022.

[24] M.-D. Wei, F. Dai, N.-W. Xu, and T. Zhao, "Stress intensity factors and fracture process zones of ISRM-suggested chevron notched specimens for mode I fracture toughness testing of rocks," *Engineering Fracture Mechanics*, vol. 168, pp. 174–189, 2016.

[25] Q. Wu, L. Weng, Y. Zhao, B. Guo, and T. Luo, "On the tensile mechanical characteristics of fine-grained granite after heating/cooling treatments with different cooling rates," *Engineering Geology*, vol. 253, pp. 94–110, 2019.

[26] M. Wei, F. Dai, Y. Liu, A. Li, and Z. Yan, "Influences of loading method and notch type on rock fracture toughness measurements: from the perspectives of t-stress and fracture process zone," *Rock Mechanics and Rock Engineering*, vol. 54, 2021.

[27] C. T. Zhou, H. P. Xie, J. B. Zhu, and T. Zhou, "Failure criterion considering high temperature treatment for rocks from a micromechanical perspective," *Theoretical and Applied Fracture Mechanics*, vol. 118, 2022.

[28] L. Zhou, L. J. Ma, Z. M. Zhu, Y. Q. Dong, J. W. Huang, and S. H. Cui, "Study of the coupling effect of elliptical cavities and cracks on tunnel stability under dynamic loads," *Theoretical and Applied Fracture Mechanics*, vol. 121, 2022.

[29] A. Zolfaghari, A. Sohrabi Bidar, M. R. Maleki Javan, M. Haftani, and A. Mehinrad, "Evaluation of rock mass improvement due to cement grouting by Q-system at Bakhtiary dam site," *International Journal of Rock Mechanics and Mining Sciences*, vol. 74, pp. 38–44, 2015.

[30] Q. Wu, L. Weng, Y. Zhao, F. Zhao, W. Peng, and S. Zhang, "Deformation and cracking characteristics of ring-shaped granite with inclusion under diametrical compression," *Arabian Journal of Geosciences*, vol. 13, 2020.

[31] Z. G. Xia, S. J. Chen, X. Z. Liu, and R. Sun, "Strength characteristics and fracture evolution of rock with different shapes inclusions based on particle flow code," *Geomechanics and Engineering*, vol. 22, pp. 461–473, 2020.

[32] K. Zhang, X. H. Liu, W. L. Liu, and S. Zhang, "Influence of weak inclusions on the fracturing and fractal behavior of a jointed rock mass containing an opening: experimental and numerical studies," *Computers and Geotechnics*, vol. 132, Article ID 104011, 2021.

[33] M. Sharafisafa, L. Shen, Y. Zheng, and J. Xiao, "The effect of flaw filling material on the compressive behaviour of 3D printed rock-like discs," *International Journal of Rock Mechanics and Mining Sciences*, vol. 117, pp. 105–117, 2019.

[34] M. El Tani, "Grouting rock fractures with cement grout," *Rock Mechanics and Rock Engineering*, vol. 45, pp. 547–561, 2012.

[35] U. Müller, L. Miccoli, and P. Fontana, "Development of a lime based grout for cracks repair in earthen constructions," *Construction and Building Materials*, vol. 110, pp. 323–332, 2016.

[36] Q. Liu, G. Lei, X. Peng, C. Lu, and L. Wei, "Rheological characteristics of cement grout and its effect on mechanical properties of a rock fracture," *Rock Mechanics and Rock Engineering*, vol. 51, pp. 613–625, 2018.

[37] X. Zhuang, J. Chun, and H. Zhu, "A comparative study on unfilled and filled crack propagation for rock-like brittle material," *Theoretical and Applied Fracture Mechanics*, vol. 72, pp. 110–120, 2014.

[38] C.-X. She and F.-T. Sun, "Study of the peak shear strength of a cement-filled hard rock joint," *Rock Mechanics and Rock Engineering*, vol. 51, pp. 713–728, 2018.

[39] Q. Q. Zhu, D. Y. Li, Z. Y. Han, X. B. Li, and Z. L. Zhou, "Mechanical properties and fracture evolution of sandstone specimens containing different inclusions under uniaxial compression," *International Journal of Rock Mechanics and Mining Sciences*, vol. 115, pp. 33–47, 2019.

[40] Q. Li, Z. Li, and X. Xu, "Experimental study for the effect of fillings on properties of brittle rock containing two parallel flaws," *Geotechnical & Geological Engineering*, vol. 38, pp. 3643–3651, 2020.

[41] X. Chang, Y. Deng, Z. H. Li, S. R. Wang, and C. A. Tang, "Crack propagation from a filled flaw in rocks considering the infill influences," *Journal of Applied Geophysics*, vol. 152, pp. 137–149, 2018.

[42] Y. Tian, Q. Liu, H. Ma, Q. Liu, and P. Deng, "New peak shear strength model for cement filled rock joints," *Engineering Geology*, vol. 233, pp. 269–280, 2018.

[43] P.-Z. Pan, S. Miao, Q. Jiang, Z. Wu, and C. Shao, "The influence of infilling conditions on flaw surface relative displacement induced cracking behavior in hard rock," *Rock Mechanics and Rock Engineering*, vol. 53, pp. 4449–4470, 2020.

[44] Z. B. Zhong, R. G. Deng, J. Zhang, and X. Z. Hu, "Fracture properties of jointed rock infilled with mortar under uniaxial compression," *Engineering Fracture Mechanics*, vol. 228, 2020.

[45] Z. L. Zhao, H. W. Jing, and X. S. Shi, "Experimental investigation and numerical modelling on strength and fracture behaviors of sandstone with weak distributed inclusions," *Geotechnical & Geological Engineering*, vol. 39, pp. 2521–2531, 2021.

[46] H. M. Tian, W. Z. Chen, D. S. Yang, and J. P. Yang, "Experimental and numerical analysis of the shear behaviour of cemented concrete–rock joints," *Rock Mechanics and Rock Engineering*, vol. 48, pp. 213–222, 2015.

[47] Y. Lu, L. Wang, Z. Li, and H. Sun, "Experimental study on the shear behavior of regular sandstone joints filled with cement grout," *Rock Mechanics and Rock Engineering*, vol. 50, pp. 1321–1336, 2017.

[48] M. H. Salimian, A. Baghbanan, H. Hashemolhosseini, M. Dehghanipoodeh, and S. Norouzi, "Effect of grouting on shear behavior of rock joint," *International Journal of Rock Mechanics and Mining Sciences*, vol. 98, pp. 159–166, 2017.

[49] C. Butron, M. Axelsson, and G. Gustafson, "Silica sol for rock grouting: Laboratory testing of strength, fracture behaviour and hydraulic conductivity," *Tunnelling and Underground Space Technology*, vol. 24, pp. 603–607, 2009.

[50] S. T. Miao, P. Z. Pan, Z. H. Wu, S. J. Li, and S. K. Zhao, "Fracture analysis of sandstone with a single filled flaw under uniaxial compression," *Engineering Fracture Mechanics*, vol. 204, pp. 319–343, 2018.

[51] M. R. Du, H. W. Jing, H. J. Su, T. T. Zhu, and M. L. Chen, "Strength and failure characteristics of sandstone containing two circular holes filled with two types of inclusions under uniaxial compression," *Journal of Central South University*, vol. 24, pp. 2487–2495, 2017.

[52] X. Chang, J. Tang, G. Z. Wang, and C. N. Tang, "Mechanical performances of rock-like disc containing circular inclusion

subjected to diametral compression," *Archives of Civil and Mechanical Engineering*, vol. 18, pp. 356–370, 2018.

[53] X. Li, Q. Wu, M. Tao, L. Weng, L. Dong, and Y. Zou, "Dynamic Brazilian splitting test of ring-shaped specimens with different hole diameters," *Rock Mechanics and Rock Engineering*, vol. 49, pp. 4143–4151, 2016.

[54] X. Zhang, Y. Yi, H. Zhu et al., "Measurement of tensile strength of nuclear graphite based on ring compression test," *Journal of Nuclear Materials*, vol. 511, pp. 134–140, 2018.

[55] D. Y. Li, T. Wang, T. J. Cheng, and X. L. Sun, "Static and dynamic tensile failure characteristics of rock based on splitting test of circular ring," *Transactions of Nonferrous Metals Society of China*, vol. 26, pp. 1912–1918, 2016.

[56] A. T. Procopio, A. Zavaliangos, and J. C. Cunningham, "Analysis of the diametrical compression test and the applicability to plastically deforming materials," *Journal of Materials Science*, vol. 38, pp. 3629–3639, 2003.

[57] J. H. Ye, F. Q. Wu, and J. Z. Sun, "Estimation of the tensile elastic modulus using Brazilian disc by applying diametrically opposed concentrated loads," *International Journal of Rock Mechanics and Mining Sciences*, vol. 46, pp. 568–576, 2009.

[58] A. Z. Lu, S. J. Wang, and H. Cai, "Closed-form solution for the stresses in Brazilian disc tests under vertical uniform loads," *Rock Mechanics and Rock Engineering*, vol. 51, pp. 3489–3503, 2018.

[59] D. J. Guerrero-Miguel, M. I. Alvarez-Fernandez, C. C. Garcia-Fernandez, C. Gonzalez-Nicieza, and C. Menendez-Fernandez, "Analytical and numerical stress field solutions in the Brazilian Test subjected to radial load distributions and their stress effects at the centre of the disk," *Journal of Engineering Mathematics*, vol. 116, pp. 29–48, 2019.